Porous Core−Shell Fe₃C Embedded N-doped Carbon Nanofibers as an Effective Electrocatalysts for Oxygen Reduction Reaction

Guangyuan Ren,[†,‡] Xianyong Lu,*[,†] Yunan Li,[†] Ying Zhu,*[,†] Liming Dai,[§] and Lei Jiang[†]

[†]Key Laboratory of Bio-inspired Smart Interfacial Science and Technology of Ministry of Education, School of Chemistry and Environment, Beihang University, Beijing 100191, People's Republic of China

[‡]School of Chemistry, Biology and Material Science, East China University of Technology, Nanchang, Jiangxi 330013, China

[§]Department of Macromolecular Science and Engineering, Case Western Reserve University, Cleveland, Ohio 44106, United States

Ⓢ *Supporting Information*
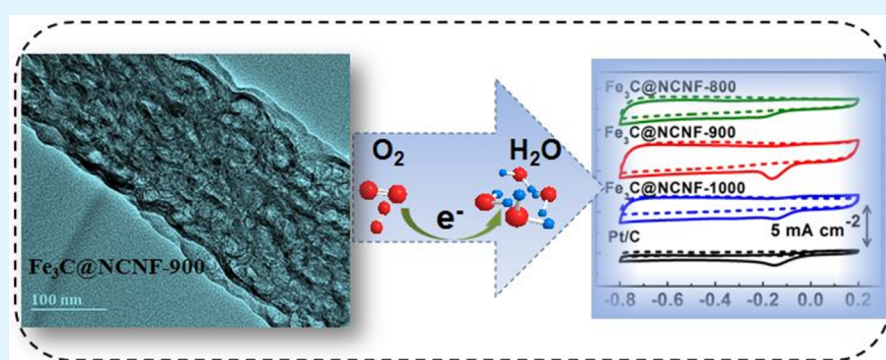
ABSTRACT: The development of nonprecious-metal-based electrocatalysts with high oxygen reduction reaction (ORR) activity, low cost, and good durability in both alkaline and acidic media is very important for application of full cells. Herein, we developed a facile and economical strategy to obtain porous core−shell Fe₃C embedded nitrogen-doped carbon nanofibers (Fe₃C@NCNF-X, where X denotes pyrolysis temperature) by electrospinning of polyvinylidene fluoride (PVDF) and FeCl₃ mixture, chemical vapor phase polymerization of pyrrole, and followed by pyrolysis of composite nanofibers at high temperatures. Note that the FeCl₃ and polypyrrole acts as precursor for Fe₃C core and N-doped carbon shell, respectively. Moreover, PVDF not only plays a role as carbon resources, but also provides porous structures due to hydrogen fluoride exposure originated from thermal decomposition of PVDF. The resultant Fe₃C@NCNF-X catalysts, particularly Fe₃C@NCNF-900, showed efficient electrocatalytic performance for ORR in both alkaline and acidic solutions, which are attributed to the synergistic effect between Fe₃C and N-doped carbon as catalytic active sites, and carbon shell protects Fe₃C from leaching out. In addition, the Fe₃C@NCNF-X catalyst displayed a better long-term stability, free from methanol crossover and CO-poisoning effects than those of Pt/C, which is of great significance for the design and development of advanced electrocatalysts based on nonprecious metals.

KEYWORDS: electrospinning, vapor phase polymerization, core−shell structure, Fe₃C, oxygen reduction reaction

1. INTRODUCTION

Oxygen reduction reaction (ORR) is a critical cathodic process in electrochemical energy conversion and storage devices, especially fuel cells and metal/air batteries.[1,2] Although Pt-based electrocatalysts have been commonly used to catalyze the ORR with high efficiency, they still suffer from several serious problems, including its high cost and the limited natural resources, together with the methanol-crossover and CO-poisoning effects, which have impeded the large-scale commercialization of fuel cells and air−metal batteries.[3,4] Therefore, it is imperative to explore low cost, high efficiency, and nonprecious-metal electrocatalysts for ORR.[5,6] Among various electrocatalysts studied so far, the iron-based nitrogen-doped carbon (Fe−N−C) catalysts are considered to be the promising candidates for ORR, due to their high activity and stability, free from the methanol-crossover and CO-poisoning

effects.[7−9] For instance, Lefèvre et al.[10] produced microporous carbon-supported iron-based N-doped catalysts by pyrolysis of a ball-milled mixture of carbon support, phenanthroline, and ferrous acetate, which showed high-efficiency ORR activity in polymer electrolyte fuel cells. Despite recent progress in Fe-based N-carbon compounds for ORR, the design and synthesis the Fe−N−C catalysts with porous architectures that offers a high surface area for fast mass transport and a large number of active sites for effective catalytic reactions still remain a challenge.

So far, nanostructured polyaniline (PANI), poly(3,4-ethylenedioxythiophene) (PEDOT), and polypyrrole (PPy) have

been used as promising precursors for the development of N-doped carbon electrocatalysts owing to their easy synthesis, various structures, and ability to generate N-contained active ORR sites.[11−15] For instance, Guo et al.[12] developed a one-step triphase self-assembling method to produce hemin-doped PEDOT with controllable three-dimensional hierarchical structures, in which the ORR-active PEDOT served also as a conductive medium, after the hemin-doping, to support the Fe−N_4-C ORR reactive centers. Zelenay et al.[15] prepared Fe−N−C ORR catalysts using high-temperature pyrolysis of PANI as precursor for carbon and nitrogen resources, which demonstrated an enhanced ORR catalytic activity with a dominant four-electron transfer process in alkaline medium. It was found that these Fe−N−C ORR catalysts have been used to facilitate oxygen reduction in alkaline medium, but not in acidic medium, because they suffer from the catalytic activity degradation due to leaching loss of transition metal caused by acid. Therefore, it is important to develop high-performance electrocatalysts for ORR in both alkaline and acidic media from the viewpoint of practical applications.

Recent research has demonstrated that the core−shell structured electrocatalysts consisting of transition metal carbide core and the graphitic carbon shell displayed significantly enhanced electrocatalytic activity toward ORR under both alkaline and acidic conditions,[16,17] in which carbon shell protects the metal core from contacting the acid electrolyte. For instance, Li et al.[17] reported that a novel type of ORR catalysts showed hollow spherical morphologies containing Fe_3C nanoparticles encased by uniform graphitic layers, which were prepared by treatment of cyanamide and ferrocene in a nitrogen-filled glovebox, then high-pressure pyrolysis. The ORR catalysts displayed excellent ORR activities and high stabilities in both acidic and alkaline media, which were attributed to the synergetic effects of active sites originated from the Fe_3C in core Fe/Fe_3C and graphitic-N species in N-doped carbon shell, and the protection of carbon shell, respectively. Therefore, the development of facile strategy for rational design the Fe_3C-based core−shell structured electrocatalysts with improved ORR performance is highly desirable for their commercial applications in the field of fuel cells and air-metal batteries.

Here, we developed a simple and economical trick to fabricate a porous core−shell Fe_3C embedded N-doped carbon nanofibers (denoted as Fe_3C@NCNF-X, where X denoted as pyrolysis temperature), via electrospinning of polyvinylidene fluoride (PVDF) and $FeCl_3$ mixture, chemical vapor phase polymerization (VPP) of pyrrole, then followed by pyrolysis under nitrogen atmosphere. $FeCl_3$ was used as not only oxidant for polymerization of pyrrole on the surface of PVDF nanofibers but also source of the iron to form Fe_3C active species toward ORR. The incorporation into PVDF had benefits in not only providing carbon sources, but also introducing abundant nanopores due to hydrogen fluoride exposure derived from thermal degradation of partial PVDF.[18,19] PPy layer on surface of electrospun fibers acted as not only precursor for active N species, but a carbon shell to protect Fe_3C core against performance decay caused by low pH. As expected, the Fe_3C@NCNF-900 exhibited a high ORR electrocatalytic performance in alkaline medium with a positive onset and reduction potential of −0.035 and −0.121 V, and a high diffusion-limited current density (4.51 mA cm^{-2}) compared to those of Pt/C catalyst (−0.032, −0.154 V, 4.93 mA cm^{-2}). At the same time, the Fe_3C@NCNF-900 catalyst

also displayed ORR activities in an acidic medium. Moreover, the resultant catalysts showed better electrocatalytic performances for ORR with a long-term stability, free from methanol crossover and CO-poisoning effects. This work provides a simple way for potential mass production of the core−shell structured electrocatalysts with high ORR performance in both alkaline and acidic media.

2. EXPERIMENTAL SECTION

2.1. Chemicals and Materials. Pyrrole (TCI Co.) was distilled under reduced pressure before use. Ferric chloride ($FeCl_3$) was purchased from Guangdong Guanghua Sci-Tech Co., Ltd. Commercial carbon-supported Pt catalyst (20 wt %, Pt/C) was obtained from Alfa Aesar. Nafion (DuPont, 10 wt %) was diluted to 0.05 wt % using ethanol. PVDF (M_w = 530 000) was supplied by Arkema. Ultrapure water (18.2 MΩ cm) was acquired by using a Millie-Q water purification system from Millipore. Unless otherwise specified, all other reagents were analytical grade and used without further purification.

2.2. Characterization. The morphologies of the Fe_3C@NCNF-X catalysts were studied with a field emission scanning electron microscope (FE-SEM, JEOL JSM-7500F), transmission electron microscope (TEM, JEOL JEM-2100F). The crystal and molecular structures of as-prepared catalysts were investigated by X-ray diffraction (XRD, XRD-6000) with Cu Kα radiation (λ = 1.5406 Å), and X-ray photoelectron spectroscopy (XPS) (VG ESCALAB 220i-XL instrument with a monochromatic Al Kα X-ray source). The specific surface area and pore size distribution were derived from nitrogen adsorption/desorption isotherm (Micromeritics ASAP 2020 V3.00 H) by using Brunauer−Emmett−Teller (BET) and Barrett−Joyner−Halenda (BJH) methods, respectively. Raman spectra were recorded on a Jobin Yvon (Laboratory RAM HR1800) confocal micro-Raman spectrometer with a backscattered geometry through a 10× (NA = 0.25) microscope objective. Ar$^+$ laser emitting at a wavelength of 633 nm was used as a source of excitation.

2.3. General Preparation Procedure for Electrocatalysts of Fe_3C@NCNF-X. First, the PVDF/$FeCl_3$ fibers were fabricated by electrospinning. $FeCl_3$ solution (3 wt %) was prepared by dissolving $FeCl_3$ in a mixture of N,N-dimethylformamide (DMF) and acetone (1:1 wt %) under ultrasonic treatment for 0.5 h, then 10 wt % PVDF was added to the solution mentioned above with stirring at least 3 h to form a homogeneous mixed solution. And then, the mixed solution was loaded into plastic syringe with a stainless-steel needle that was connected to a high voltage power supply (FL 32174, Gamma). A positive voltage of 20 kV was applied and a piece of aluminum foil was placed 20 cm below the tip of the needle to collect the PVDF/$FeCl_3$ fibers, then the fibers membrane was eventually placed in a vacuum oven at 60 °C for 10 h. Second, PVDF/$FeCl_3$@PPy core−shell fiber was fabricated by the vapor phase polymerization (VPP) of pyrrole in the presence of PVDF/$FeCl_3$ fibers as substrates. Finally, the black PVDF/$FeCl_3$@PPy core−shell fiber films were annealed in tubular furnace under argon atmosphere at 800, 900, and 1000 °C for 2 h with a heating rate of 5 °C min^{-1} and cooled down naturally. According to the pyrolysis temperature, the as-prepared catalysts were denoted as Fe_3C@NCNF-800, Fe_3C@NCNF-900, Fe_3C@NCNF-1000, respectively.

2.4. Electrochemical Measurements. The electrochemical properties of the samples were measured on a CHI 760D (Chenhua, Shanghai) with three electrode cell. A platinum wire and a saturated Hg|Hg_2Cl_2 (KCl sat.) were used as the counter electrodes, reference electrode, respectively. Glass carbon (GC) disk of 5 mm in diameter was used as the working electrode for the catalyst materials. 0.1 M KOH and 0.1 M $HClO_4$ aqueous solution were the electrolytes, which was saturated with pure nitrogen or oxygen gas for 30 min prior to the electrochemical test. The working electrodes were prepared by applying the catalyst ink onto a prepolished GC disk electrode. Briefly, the catalyst was dispersed in ethanol and ultrasonicated for 1 h to form a homogeneous catalyst ink (2 mg mL^{-1}). Then, 15 μL of catalyst ink was applied on the GC electrode. After drying at room

temperature, 15 μL of Nafion (0.05 wt %) solution in ethanol was applied on the surface of the catalyst layer to form a thin protective film. For comparison, the Pt/C (20 wt % Pt) electrode with the same amount of catalyst loading was used. The ORR activity was evaluated by cyclic voltammetry (CV) and linear sweep voltammetry (LSV) techniques on rotating disk electrode (RDE) in O_2-saturated 0.1 M KOH and 0.1 M $HClO_4$ electrolytes. The chronoamperometric current−time (i−t) method was used to investigate the electrode stability at the bias potential of −0.2 V (vs Hg|Hg$_2$Cl$_2$) in O_2-saturated 0.1 M KOH solutions with a rotation rate of 900 rpm. Then, the tolerance to the methanol crossover and CO poisoning effects were tested by adding 5 mL methanol and 60 mL min^{-1} continuous CO gas into the O_2-saturated electrochemical cell.

3. RESULTS AND DISCUSSION

The fabrication procedure for porous core−shell Fe$_3$C@NCNF-X is illustrated in Scheme 1. First, PVDF/FeCl$_3$

Scheme 1. Schematic Illustration of the Fabrication of thFe$_3$C@NCNF-X Nanofibers
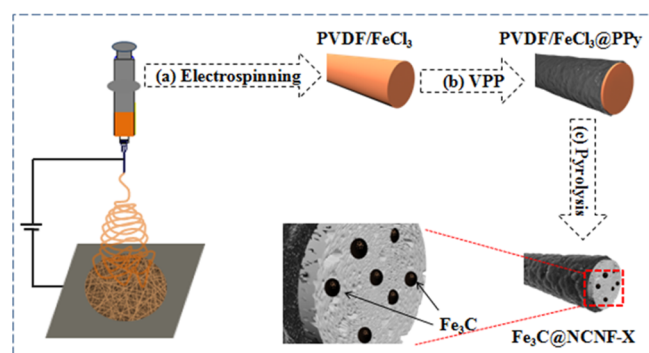
^{a}Electrospinning of PVDF and FeCl$_3$ mixture to obtain PVDF/FeCl$_3$ nanofibers. ^{b}VPP of pyrrole to form PPy shell on the surface of PVDF/FeCl$_3$ nanofibers. ^{c}Pyrolysis of PVDF/FeCl$_3$@PPy to obtain Fe$_3$C@NCNF-X nanofibers.

nanofibers were obtained by electrospinning of PVDF and FeCl$_3$ mixture. Second, PVDF/FeCl$_3$@PPy fiber was fabricated by vapor-phase polymerization (VPP) of pyrrole on the surface of PVDF/FeCl$_3$ nanofibers. Third, the pyrolysis of PVDF/FeCl$_3$@PPy nanofibers was performed under nitrogen atmosphere at 800, 900, and 1000 °C, respectively. Finally, the as-prepared Fe$_3$C embedded N-doped carbon nanofibers (denoted as Fe$_3$C@NCNF-X) with porous structures were obtained.

Figure 1 and Figure S1 showed the scanning electron microscopy (SEM) images of the electrospun PVDF/FeCl$_3$, PVDF/FeCl$_3$@PPy and Fe$_3$C@NCNF-X nanofibers. PVDF/FeCl$_3$ nanofibers exhibited a smooth surface with an average diameter of 395 ± 24 nm, as shown in Figure 1a and Figure S1a. The color of PVDF/FeCl$_3$ nanofibers was faint yellow due to the presence of FeCl$_3$ (inset of Figure 1a). After the VPP, the surface of PVDF/FeCl$_3$@PPy nanofibers became slightly rough, and the average diameter increases to 409 ± 29 nm (Figure 1b and Figure S1b). Moreover, the color of PVDF/FeCl$_3$@PPy nanofibers changed to black owing to the formation of PPy layer on the surface of the PVDF/FeCl$_3$ nanofibers (inset of Figure 1b). As shown in Figure 1c, the average diameter Fe$_3$C@NCNF-900 nanofibers decreased to 378 ± 23 nm. From the enlarged SEM image in Figure 1d, it can be seen that the Fe$_3$C@NCNF-900 nanofibers revealed rough structures due to the thermal decomposition of polymers. Moreover, Fe$_3$C@
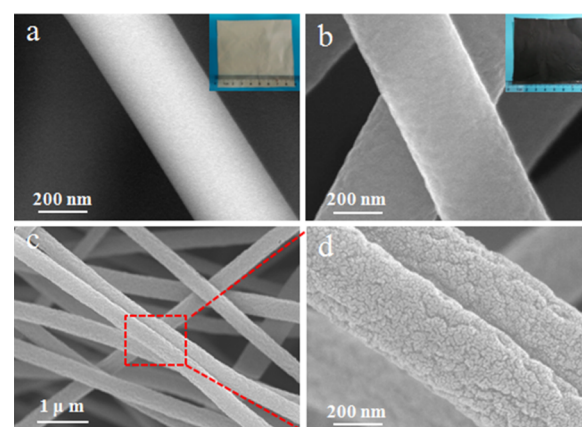
Figure 1. SEM images of (a) PVDF/FeCl$_3$ nanofibers, (b) PVDF/FeCl$_3$ nanofibers coated with PPy shell, (insets) corresponding digital photograph, and (c, d) Fe$_3$C@NCNF-900 nanofibers with different magnifications.

NCNF-800 and Fe$_3$C@NCNF-1000 nanofibers also displayed rough surface, and their average diameters were respectively 387 ± 36 and 356 ± 28 nm, as given in Figure S1c−f. The diameter of Fe$_3$C@NCNF-X nanofibers decreased slightly with the increasing pyrolysis temperature, even a few of them broke down at 1000 °C, because high temperature caused more thermal degradation of PVDF and PPy in the nanofibers.

Morphology of Fe$_3$C@NCNF-X was further studied using high-resolution transmission electron microscopy (HRTEM) and the corresponding selected area electron diffraction (SAED). In Figure 2a, Fe$_3$C@NCNF-900 nanofibers displayed

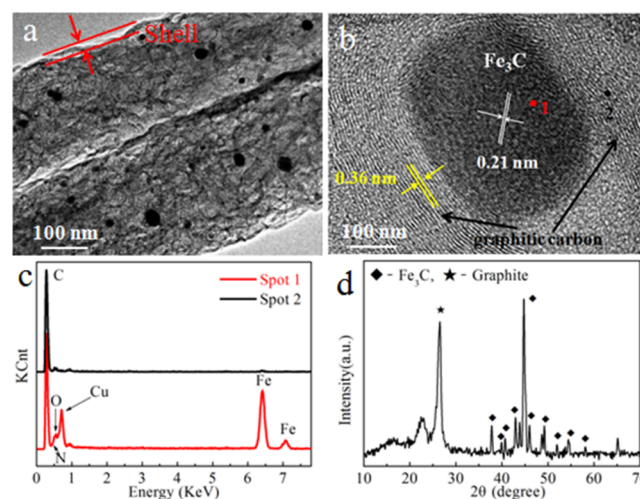**Figure 2.** (a, b) HRTEM images, (c) corresponding EDS spectrum of the Fe$_3$C@NCNF-900 nanofibers from panel b, and (d) XRD of the Fe$_3$C@NCNF-900 nanofibers.

porous core−shell structures with an average shell thickness of about 20 nm. HRTEM of the Fe$_3$C@NCNF-800 and the Fe$_3$C@NCNF-1000 nanofibers in Figure S5 obviously showed the shell structures as marked by red arrows, which are consistent well with the core−shell structure of Fe$_3$C@NCNF-900 nanofibers. The nanoparticles with an average diameter of 17 ± 1.5 nm were embedded into the Fe$_3$C@NCNF-900 nanofibers, whose size distribution of the nanoparticles was shown in Figure S2a. The HRTEM images in Figure 2b and Figure S2b further demonstrated that the nanoparticles were

enclosed by graphitic carbon shells, the spacing of crystalline lattices was 0.21 nm, corresponding to the (211) planes of the Fe_3C phase.[16] It can been seen from Figure S2c that the corresponding SAED pattern showed regular scattered dots, indicating that the core Fe_3C bore a single crystalline structure.[20] As shown in Figure 2c, the energy-dispersive X-ray spectroscopy (EDS) spectrum confirmed that the nanoparticle was composed of C and Fe elements (marked by the red Spot 1 in Figure 2b), which was attributed to catalytic active of Fe ions on graphitization. The portion outside of nanoparticle was only made of C element (marked by the black Spot 2 in Figure 2b), while the signals of Cu originated from the supporting copper grid. The content of elements based on EDS of Fe_3C@NCNF-900 nanofibers was summarized in Table S1 of Supporting Information. The crystal structure of Fe_3C@NCNF-900 nanofibers was further characterized by X-ray diffraction (XRD). The XRD pattern of Fe_3C@NCNF-900 sample (Figures 2d), provided a typical strong peak at about 26°, corresponding to the (002) facets of graphite carbon. The peaks located at 37.8, 43.9, 45.0, 46.0, 49.2, and 54.5° were indexed to the Fe_3C (JCPDS file no. 892867), which was consistent with the results of HRTEM, SAED and EDS. The above results verified that the Fe_3C nanoparticles were wrapped by graphitic carbon layer. Recent reports demonstrated that the wrapped metal-based nanoparticles could generate a unique host−guest electronic interaction and change the local work function of the graphitic carbon sheets, making the outer surface of the carbon layer more active to ORR.[17,21]

Brunauer−Emmett−Teller (BET) surface area and pore size distribution were obtained from a N_2 adsorption−desorption analysis. As shown in Figure 3a, all the Fe_3C@NCNF-X samples displayed the type IV isotherm that was characteristic of mesoporous materials. A multiple mesoporous structures were observed in corresponding pore size distribution curves of the Fe_3C@NCNF-800, -900, and -1000 (inset in Figure 3a), it can be seen that the pores for these three samples were

unimodal with average pore sizes of 3.9, 4.0, and 4.2 nm, respectively. The Fe_3C@NCNF-900 nanofibers exhibited the largest BET surface area of 360.6 m^2 g^{-1} compared to 247.7 m^2 g^{-1} for Fe_3C@NCNF-800 and 324.0 m^2 g^{-1} for Fe_3C@NCNF-1000. It can be concluded that increasing treatment temperature from 800 to 900 °C significantly increases the specific surface area. But further increasing temperature leads to a slight decrease in the specific surface area, which may be attributed to the partial destruction of ordered mesopores.[8,16] It was considered that the high-surface-area materials would introduce more active sites, thus improving the catalytic ORR activity. Moreover, the mesoporosity has generally been demonstrated to promote the accessibility to catalytic active sites for ORR-related species.[22,23] The Fe_3C@NCNF-900 sample had the largest surface area and suitable mesoporosity systems and was therefore expected to display good ORR performance.

The molecular structures of the as-prepared Fe_3C@NCNF-X were investigated using the Raman spectra. The Raman spectra of Fe_3C@NCNF-800, Fe_3C@NCNF-900, and Fe_3C@NCNF-1000 (Figure 3b), showed the well-documented D band at 1326 cm^{-1} and G band at 1590 cm^{-1}, corresponding with the disordered graphitic carbon and the vibration of the sp^2-bonded carbon atoms in a two-dimensional hexagonal lattice, respectively, which indicated that graphitic carbon formed during pyrolysis at high-temperature.[16,24] The ratio of integrated intensity of the D and G band (I_D/I_G) is widely used to assess the density of defects in graphite materials. It was observed that the I_D/I_G values were 1.27 for Fe_3C@NCNF-800, 1.25 for Fe_3C@NCNF-900 and 1.22 for Fe_3C@NCNF-1000, respectively, indicating that the graphitization degree of Fe_3C@NCNF-X is promoted with the increasing pyrolysis temperatures.

X-ray photoelectron spectroscopy (XPS) was carried out to determine the surface elements, which provided more detailed information about the chemical compositions of Fe_3C@NCNF-X, as shown in Figure 4 and Figure S3. The survey XPS spectrum of the Fe_3C@NCNF-X revealed the presence of C, O, N, and Fe, demonstrating that N and Fe were successfully incorporated into the carbon framework, whereas the level of
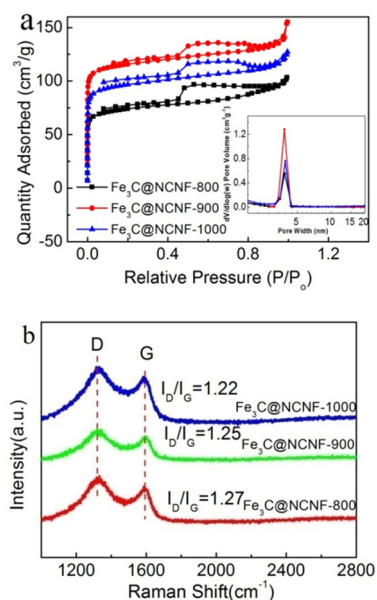

Figure 3. (a) N_2 adsorption−desorption isotherm, (inset) corresponding pore size distribution curves of the Fe_3C@NCNF-X and (b) Raman spectra of the Fe_3C@NCNF-X.
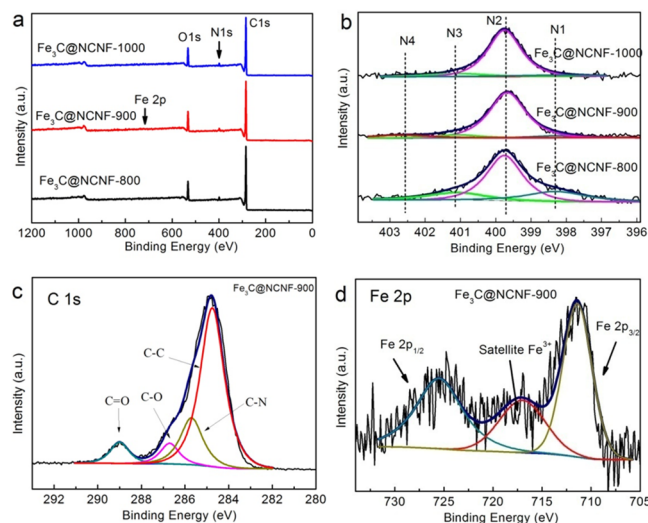

Figure 4. (a) Survey XPS spectrum of the Fe_3C@NCNF-X nanofibers, (b) N 1s spectrum of the Fe_3C@NCNF-X nanofibers, (c) C 1s, (d) Fe 2p spectrum of the Fe_3C@NCNF-900 nanofibers, together with their corresponding fits.

Fe elements detected in catalysts was low, which might be resulted from the coverage of graphitic layers on the Fe_3C surface. Nitrogen content in catalysts was respectively measured to be 2.48 atom % for Fe$_3$C@NCNF-800, 2.12 atom % for Fe$_3$C@NCNF-900, 1.81 atom % for Fe$_3$C@NCNF-1000, which slightly reduced with increasing pyrolysis temperature, due to more decomposition of PPy. Figure 4b displayed high-resolution N 1s spectra of the as-fabricated Fe$_3$C@NCNF-X, which can be further deconvoluted into four peaks corresponding to pyridinic N (398.4 eV), pyrrolic N (399.8 eV), quaternary N (401.2 eV), and oxidized N (402.6 eV). Recently, previous reports have demonstrated that all of the pyridinic N, pyrrolic N, and quaternary N can increase current density and boost oxygen reduction, except the uncertain contribution of the oxidized N.[7,25,32] Pyridinic N donates one p-electron donor, which has long pair of electrons for binding with metal atoms.[26] Pyrrolic N and quaternary N are two p-electron donors, which could increase catalytic activity via lowering the carbon band gap energy, compared with oxidized N and pyridinic N, the pyrrolic N could exhibit a higher charge mobility and better donor−acceptor charge transfer capability.[26−28] The N 1s XPS spectra showed the highest amount of pyrrolic N in the Fe$_3$C@NCNF-X catalysts, the values were 66.09, 84.38, and 83.64 atom % at the temperature of 800, 900, and 1000 °C, respectively. Thus, the highest amount of pyrrolic N in the Fe$_3$C@NCNF-900 catalyst has an important contribution for promotion of the ORR performance. The XPS C 1s high-resolution spectrum of the Fe$_3$C@NCNF-900 can be deconvoluted into the sp^2 hybridized C atom in graphene (284.8 eV),[29,30] C−N (285.7 eV), carboxyl C=O (289.0 eV), and hydroxy C−O (286.7 eV)[31] carbon bonded with oxygen (Figure 4c), which corresponded with the results the O 1s peak (Figure S3b). The XPS Fe 2p high-resolution spectrum of the Fe$_3$C@NCNF-900 given in Figure 4d showed two major peaks at 712.8 and 725.3 eV corresponding to Fe 2p^3 and Fe 2p^1, respectively, along with one weak peak due to a shakeup satellite peaks of Fe 2p^3,[16,17] confirmed existence of Fe$_3$C in as-prepared catalysts, which were in accordance with the results of HRTEM and XRD.

The electrocatalytic activity of Fe$_3$C@NCNF-X and Pt−C catalysts toward ORR was initially examined by cyclic voltammetric (CV) measurements in N$_2$ and O$_2$-saturated 0.1 M KOH aqueous solutions with a scan rate of 50 mV s^{-1}. As shown in Figure 5a (dashed curves), a quasi-rectangular voltammogram without no redox peak over a potential range from −0.8 to 0.2 V was observed for all samples tested in the N$_2$-saturated solution. In contrast, the Fe$_3$C@NCNF-900 electrode exhibited a ORR peak with an onset and peak potentials at −0.058 and −0.161 V in the O$_2$-saturated 0.1 M KOH aqueous solution, respectively, which were more positive than those of Fe$_3$C@NCNF-800 (−0.097 and −0.205 V) and comparable to Fe$_3$C@NCNF-1000 (−0.056 and −0.151 V) and commercial Pt/C catalysts (−0.032 and −0.154 V). Moreover, the Fe$_3$C@NCNF-900 catalyst even showed a higher peak current density (2.95 mA cm^{-2}) than that of the commercial Pt/C catalyst (1.44 mA cm^{-2}). These results indicated that Fe$_3$C@NCNF-900 could be used as an efficient ORR catalyst due to the largest surface area and the highest amount of ORR active sites of the Fe$_3$C nanoparticles and the pyrrolic N.[32,33]

To gain further insight into the electrocatalytic properties of Fe$_3$C@NCNF-X, linear sweeping voltammograms (LSV) measurements were carried out on a rotating disk electrode
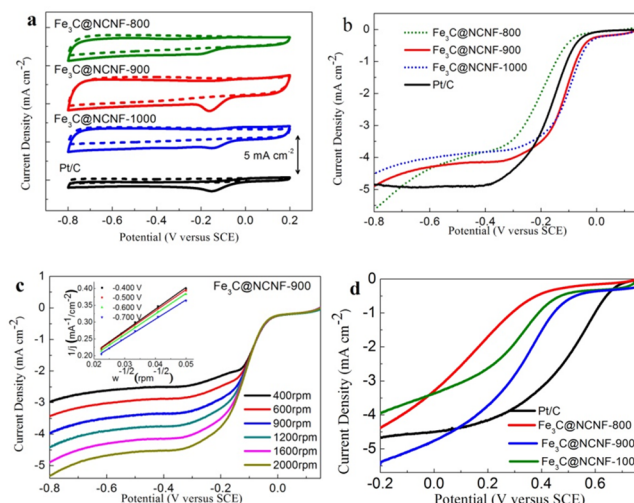

Figure 5. (a) CV curves of the Fe$_3$C@NCNF-X and Pt/C on GC electrodes in O$_2$-saturated (solid line) and N$_2$-saturated (dashed line) 0.1 M KOH at a scan rate of 50 mV s^{-1}, (b) LSV curves of the Fe$_3$C@NCNF-X and Pt/C in O$_2$-saturated 0.1 M KOH at a scan rate of 10 mV s^{-1} and a rotation rate of 1600 rpm, (c) LSV curves of the Fe$_3$C@NCNF-900 in O$_2$-saturated 0.1 M KOH solution at rotation rate from 400 to 1600 rpm, and (inset) the K−L plots of Fe$_3$C@NCNF-900 catalyst. (d) LSV curves of the Fe$_3$C@NCNF-X and Pt/C in O$_2$-saturated 0.1 M HClO$_4$ solution at a scan rate of 10 mV s^{-1} and a rotation rate of 1600 rpm.

(RDE) at a rotation rate of 1600 rpm. LSV curves of Fe$_3$C@NCNF-X and Pt/C catalysts in O$_2$-saturated 0.1 M KOH solution were shown in Figure 5b, from which the onset and half-wave ($E_{1/2}$) potentials of the Fe$_3$C@NCNF-900 catalyst were calculated to be −0.035 and −0.121 V, respectively, both of them were more positive than those of the commercial Pt/C catalyst (Table S2). The limited current density of Fe$_3$C@NCNF-900 (4.51 mA cm^{-2}) was slightly lower than that of Pt/C (4.93 mA cm^{-2}). Taken together, these results demonstrated that the catalytic ORR activity of Fe$_3$C@NCNF-900 catalyst could be comparable to commercial Pt/C catalyst.

To investigate the ORR kinetics processes of Fe$_3$C@NCNF-X catalysts, we performed the LSV measurements on a rotating disk electrode (RDE) under different rotation speeds. Generally, the electrochemical reduction of oxygen in alkaline solution included two main possible pathways: the two-electron and four-electron reduction pathway. The four-electron pathway is more efficient. The transferred electron number (n) per oxygen molecule can be calculated by Koutechy−Levich equation as given below (eq 1 and 2):

$$\frac{1}{j} = \frac{1}{j_k} + \frac{1}{j_L} = \frac{1}{j_k} + \frac{1}{B\omega^{0.5}} \tag{1}$$

$$B = 0.2nF(D_{O_2})^{2/3} v^{-1/6} C_{O_2} \tag{2}$$

where, j_k is kinetic current density, j_L is the diffusion-limited current density and ω is rotating rate. B can be determined by the slope of K−L plots based on Levich equation where n, F, D_{O_2}, ν, C_{O_2} represent the transferred electron number per oxygen molecule, Faraday constant (96485 C mol^{-1}), diffusion coefficient of O$_2$ (1.9 × 10^{-5} cm^2 s^{-1}), the kinetic viscosity (1.1 × 10^{-2} cm^2 s^{-1}), and the bulk concentration of O$_2$ (1.2 × 10^{-6} mol cm^{-3}) in 0.1 M KOH solutions, respectively. The constant 0.2 is adopted when the rotation speed is expressed in rpm.[12]

From Figure 5c, it can be seen that the diffusion current densities for Fe₃C@NCNF-900 catalyst depended on the rotating rates, and thus a diffusion-controlled oxygen reduction reaction can be verified. Based on the Koutecky−Levich (K−L) equations and K−L plots (inset of Figure 5c), the transferred electrons number (n) in the reduction process was calculated to be 3.8 at −0.50 V for Fe₃C@NCNF-900, indicating that the ORR catalyzed by Fe₃C@NCNF-900 occurred almost entirely through the four-electron reduction pathway, close to that of 4.0 of commercial Pt/C. As for Fe₃C@NCNF-800 and Fe₃C@NCNF-1000 catalysts, the n values were 2.5 and 3.4 at −0.40 V respectively, indicating a mixed reduction pathway, as shown in Figure S4. According to these results, it can be concluded that Fe₃C@NCNF-900 can exhibit more efficient electrochemical reduction of oxygen to that of Fe₃C@NCNF-800 and Fe₃C@NCNF-1000. Figure S6 showed the Tafel plots of Fe₃C@NCNF-X and commercial Pt/C derived by the mass transport correction of corresponding LSV data in Figure 5b. Fe₃C@NCNF-900 has a Tafel slope of 81 mV decade⁻¹ in 0.10 M KOH that is very close to 78 mV decade⁻¹ of the commercial Pt/C, indicating that Fe₃C@NCNF-900 has a good kinetic process for ORR.

To investigate the electrocatalytic performance of Fe₃C@NCNF-X in acidic medium, the LSV measurements were surveyed on a RDE at a rotation rate of 1600 rpm. Figure 5d showed the LSV curves of Fe₃C@NCNF-X and Pt/C catalysts in O₂-saturated 0.1 M HClO₄ solution, from which the onset and half-wave ($E_{1/2}$) potentials of the Fe₃C@NCNF-900 catalyst were calculated to be 0.532 and 0.342 V, respectively, both of them were more positive than those of Fe₃C@NCNF-800 and Fe₃C@NCNF-1000, negative than those of Pt/C catalyst (0.685 and 0.491 V). The limited current density of Fe₃C@NCNF-900 (4.79 mA cm⁻²) was slightly higher than that of Pt/C (4.45 mA cm⁻²). It is demonstrated that the Fe₃C@NCNF-900 catalyst could display catalytic activity toward ORR in acidic solution as well, and had little difference compared with commercial Pt/C catalyst.

For the purpose of investigate the electrode stability, an accelerated degradation test was performed using the chronoamperometric current−time ($i−t$) method in an O₂-saturated 0.1 M KOH aqueous solution at −0.2 V and a rotation rate of 900 rpm. The $i−t$ curves in Figure 6a showed that the Fe₃C@NCNF-900 catalyst had a much higher stability than that of commercial Pt/C electrocatalyst. The accelerated durability experiments of Fe₃C@NCNF-900 and Pt/C were also performed by potential cycling between 0.2 to −0.6 V in O₂-saturated 0.10 M KOH solution at a rotation rate of 1600 rpm, as given in Figure S7. After 4000 cycles, Fe₃C@NCNF-900 catalyst had a degradation of 24 mV in half-wave potential, while the degradation of Pt/C catalyst was severe with a decrease of 26 mV in half-wave potential.

Compared to the Pt/C electrode, Fe₃C@NCNF-900 catalyst also showed a higher tolerance to the methanol crossover (Figure 6b). The Fe₃C@NCNF-900 showed a weak CO-poisoning effect, while the current of the Pt/C electrode displayed a remarkable decay (Figure 6c). These stabilities of Fe₃C@NCNF-900 catalysts were attributed to protection of the graphitic carbon sheets against the properties decay, indeed, which was a stable cathode ORR electrocatalyst for fuel cells.

4. CONCLUSION

In summary, we have developed a simple strategy for the fabrication of porous core−shell Fe₃C/nitrogen-doped carbon
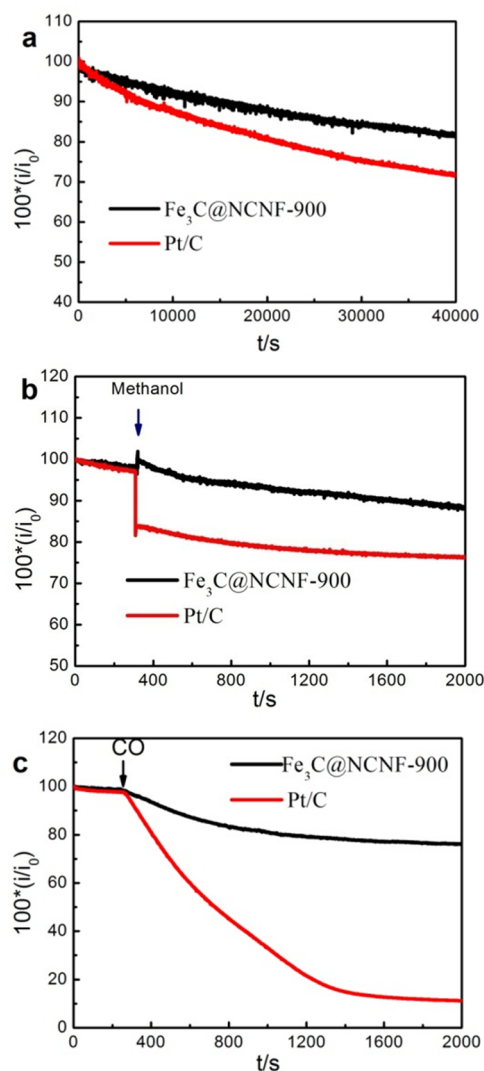

Figure 6. (a) Durability evaluation from the current−time ($i−t$) chronoamperometric responses of the Fe₃C@NCNF-900 catalyst and commercial Pt/C electrodes in O₂-saturated KOH (0.1 M) aqueous solution at −0.2 V and a rotation rate of 900 rpm, (b) I-t curves for the methanol-crossover effect, (c) I-t curves for CO-poison effect, the arrows indicated that the addition 5 mL methanol into the O₂-saturated electrochemical cell after about 300 s and 60 mL min⁻¹ continuous CO gas into the electrochemical cell saturated by O₂ flow at 300 s.

nanofibers (Fe₃C@NCNF-X) by combining electrospinning, VPP and pyrolysis process. It was found that both FeCl₃ and polypyrrole acted as resources to created Fe₃C and pyrrolic-N active sites toward ORR in Fe₃C@NCNF-X catalysts. Importantly, the Fe₃C@NCNF-900 catalysts exhibited a high catalytic ORR activity in alkalic media, and a suited catalytic ORR activity in acidic medium. In addition, the Fe₃C@NCNF-900 catalysts exhibited better stability, better methanol and CO tolerance abilities for ORR than those of commercial Pt/C catalyst in 0.10 M KOH solution. We proposed that the synergetic effects between core-Fe₃C and pyrrolic N-doped graphite, combined with porous structures providing the improvement of the electrocatalysts performance for ORR.[16,20] In addition, the carbon shell could protect against the performance degradation and provided a high catalytic stability of Fe₃C@NCNF-900. Considering the facile and mass

production synthesis and efficient ORR performance, $Fe_3C@$NCNF-900 catalyst would be a promising alternative to Pt/based catalysts for application in electrochemical energy conversion.

■ ASSOCIATED CONTENT

Ⓢ Supporting Information

The Supporting Information is available free of charge on the ACS Publications website at DOI: 10.1021/acsami.5b11786.

> SEM images of the $Fe_3C@$NCNF-X, size distribution of Fe_3C particles, HRTEM of the $Fe_3C@$NCNF-900, and the corresponding selected area electron diffraction pattern. LSV curves of the $Fe_3C@$NCNF-X and Pt/C, the K−L plots of corresponding catalysts. Table of electrochemical parameters for ORR estimated from CVs and LSV curves. (PDF)

■ AUTHOR INFORMATION

Corresponding Authors
*E-mail: xylu@buaa.edu.cn.
*E-mail: zhuying@buaa.edu.cn.

Notes
The authors declare no competing financial interest.

■ ACKNOWLEDGMENTS

■ REFERENCES

(1) Service, R. F. Shrinking Fuel Cells Promise Power in Your Pocket. *Science* **2002**, *296*, 1222−1224.

(2) Steele, B. C. H.; Heinzel, A. Materials for Fuel-Cell Technologies. *Nature* **2001**, *414*, 345−352.

(3) Morozan, A.; Jousselme, B.; Palacin, S. Low-Platinum and Platinum-Free Catalysts for the Oxygen Reduction Reaction at Fuel Cell Cathodes. *Energy Environ. Sci.* **2011**, *4*, 1238−1254.

(4) Dai, L.; Xue, Y.; Qu, L.; Choi, H. J.; Baek, J. B. Metal-Free Catalysts for Oxygen Reduction Reaction. *Chem. Rev.* **2015**, *115*, 4823−4892.

(5) Wu, G.; Zelenay, P. Nanostructured Nonprecious Metal Catalysts for Oxygen Reduction Reaction. *Acc. Chem. Res.* **2013**, *46*, 1878−1889.

(6) Singh, K. P.; Bae, E. J.; Yu, J. S. Fe-P: A New Class of Electroactive Catalyst for Oxygen Reduction Reaction. *J. Am. Chem. Soc.* **2015**, *137*, 3165−3168.

(7) Hu, Y.; Jensen, J. O.; Zhang, W.; Huang, Y.; Cleemann, L. N.; Xing, W.; Bjerrum, N. J.; Li, Q. Direct Synthesis of Fe_3C-Functionalized Graphene by High Temperature Autoclave Pyrolysis for Oxygen Reduction. *ChemSusChem* **2014**, *7*, 2099−2103.

(8) Xiao, M.; Zhu, J.; Feng, L.; Liu, C.; Xing, W. Meso/Macroporous Nitrogen-Doped Carbon Architectures with Iron Carbide Encapsulated in Graphitic Layers As an Efficient and Robust Catalyst for the Oxygen Reduction Reaction in Both Acidic and Alkaline Solutions. *Adv. Mater.* **2015**, *27*, 2521−2527.

(9) Wu, Z. S.; Yang, S.; Sun, Y.; Parvez, K.; Feng, X.; Mullen, K. 3D Nitrogen-Doped Graphene Aerogel-Supported Fe_3O_4 Nanoparticles as Efficient Electrocatalysts for the Oxygen Reduction Reaction. *J. Am. Chem. Soc.* **2012**, *134*, 9082−9085.

(10) Lefèvre, M.; Proietti, E.; Jaouen, F.; Dodelet, J. P. Iron-Based Catalysts with Improved Oxygen Reduction Activity in Polymer Electrolyte Fuel Cells. *Science* **2009**, *324*, 71−74.

(11) Winther-Jensen, B.; Winther-Jensen, O.; Forsyth, M.; Macfarlane, D. R. High Rates of Oxygen Reduction over a Vapor Phase-Polymerized PEDOT Electrode. *Science* **2008**, *321*, 671−674.

(12) Guo, Z.; Liu, H.; Jiang, C.; Zhu, Y.; Wan, M.; Dai, L.; Jiang, L. Biomolecule-Doped PEDOT with Three-Dimensional Nanostructures as Efficient Catalyst for Oxygen Reduction Reaction. *Small* **2014**, *10*, 2087−2095.

(13) Li, S.; Wu, D.; Cheng, C.; Wang, J.; Zhang, F.; Su, Y.; Feng, X. Polyaniline-Coupled Multifunctional 2D Metal Oxide/hydroxide Graphene Nanohybrids. *Angew. Chem., Int. Ed.* **2013**, *52*, 12105−12109.

(14) Yuan, X.; Zeng, X.; Zhang, H.; Ma, Z.; Wang, C. Improved Performance of Proton Exchange Membrane Fuel Cells with p-Toluenesulfonic Acid-Doped Co-PPy/C as Cathode Electrocatalyst. *J. Am. Chem. Soc.* **2010**, *132*, 1754−1755.

(15) Wu, G.; More, K. L.; Johnston, C. M.; Zelenay, P. High-Performance Electrocatalysts for Oxygen Reduction Derived from Polyaniline, Iron, and Cobalt. *Science* **2011**, *332*, 443−447.

(16) Yang, W.; Liu, X.; Yue, X.; Jia, J.; Guo, S. Bamboo-Like Carbon Nanotube/Fe_3C Nanoparticle Hybrids and Their Highly Efficient Catalysis for Oxygen Reduction. *J. Am. Chem. Soc.* **2015**, *137*, 1436−1439.

(17) Hu, Y.; Jensen, J. O.; Zhang, W.; Cleemann, L. N.; Xing, W.; Bjerrum, N. J.; Li, Q. Hollow Spheres of Iron Carbide Nanoparticles Encased in Graphitic Layers as Oxygen Reduction Catalysts. *Angew. Chem., Int. Ed.* **2014**, *53*, 3675−3679.

(18) Qiu, Y.; Yin, J.; Hou, H.; Yu, J.; Zuo, X. Preparation of Nitrogen-Doped Carbon Submicrotubes by Coaxial Eelectrospinning and Their Electrocatalytic Activity for Oxygen Reduction Reaction in Acid Media. *Electrochim. Acta* **2013**, *96*, 225−229.

(19) Liu, F.; Hashim, N. A.; Liu, Y.; Abed, M. R. M.; Li, K. Progress in the Production and Modification of PVDF Membranes. *J. Membr. Sci.* **2011**, *375*, 1−27.

(20) Wen, Z.; Ci, S.; Zhang, F.; Feng, X.; Cui, S.; Mao, S.; Luo, S.; He, Z.; Chen, J. Nitrogen-Enriched Core-Shell Structured Fe/Fe_3C-C Nanorods as Advanced Electrocatalysts for Oxygen Reduction Reaction. *Adv. Mater.* **2012**, *24*, 1399−1404.

(21) Chung, H. T.; Won, J. H.; Zelenay, P. Active and Stable Carbon Nanotube/Nanoparticle Composite Electrocatalyst for Oxygen Reduction. *Nat. Commun.* **2013**, *4*, 1922.

(22) Liang, H. W.; Zhuang, X.; Bruller, S.; Feng, X.; Mullen, K. Hierarchically Porous Carbons with Optimized Nitrogen Doping as Highly Active Electrocatalysts for Oxygen Reduction. *Nat. Commun.* **2014**, *5*, 4973−4973.

(23) Wei, W.; Liang, H.; Parvez, K.; Zhuang, X.; Feng, X.; Mullen, K. Nitrogen-Doped Carbon Nanosheets with Size-Defined Mesopores as Highly Efficient Metal-Free Catalyst for the Oxygen Reduction Reaction. *Angew. Chem., Int. Ed.* **2014**, *53*, 1570−1574.

(24) Hou, Y.; Wen, Z.; Cui, S.; Guo, X.; Chen, J. Constructing 2D Porous Graphitic C_3N_4 Nanosheets/Nitrogen-Doped Graphene/Layered MoS_2 Ternary Nanojunction with Enhanced Photoelectrochemical Activity. *Adv. Mater.* **2013**, *25*, 6291−6297.

(25) Hu, Y.; Jensen, J. O.; Zhang, W.; Martin, S.; Chenitz, R.; Pan, C.; Xing, W.; Bjerrum, N. J.; Li, Q. Fe_3C-Based Oxygen Reduction Catalysts: Synthesis, Hollow Spherical Structures and Applications in Fuel Cells. *J. Mater. Chem. A* **2015**, *3*, 1752−1760.

(26) Chung, H. T.; Johnston, C. M.; Artyushkova, K.; Ferrandon, M.; Myers, D. J.; Zelenay, P. Cyanamide-Derived Non-Precious Metal Catalyst for Oxygen Reduction. *Electrochem. Commun.* **2010**, *12*, 1792−1795.

(27) Ding, W.; Wei, Z.; Chen, S.; Qi, X.; Yang, T.; Hu, J.; Wang, D.; Wan, L. J.; Alvi, S. F.; Li, L. Space-confinement-induced Synthesis of Pyridinic- and Pyrrolic-Nitrogen-Doped Graphene for the Catalysis of Oxygen Reduction. *Angew. Chem., Int. Ed.* **2013**, *52*, 11755−11759.

(28) Unni, S. M.; Devulapally, S.; Karjule, N.; Kurungot, S. Graphene Enriched with Pyrrolic Coordination of the Doped Nitrogen as an Efficient Metal-Free Electrocatalyst for Oxygen Reduction. *J. Mater. Chem.* **2012**, *22*, 23506−23513.

(29) Li, Y.; Zhou, W.; Wang, H.; Xie, L.; Liang, Y.; Wei, F.; Idrobo, J. C.; Pennycook, S. J.; Dai, H. An Oxygen Reduction Electrocatalyst Based on Carbon Nanotube-Graphene Complexes. *Nat. Nanotechnol.* **2012**, *7*, 394−400.

(30) Luo, Z.; Lim, S.; Tian, Z.; Shang, J.; Lai, L.; MacDonald, B.; Fu, C.; Shen, Z.; Yu, T.; Lin, J. Pyridinic N Doped Graphene: Synthesis, Electronic Structure, and Electrocatalytic Property. *J. Mater. Chem.* **2011**, *21*, 8038−8044.

(31) Song, S.; Xue, Y.; Feng, L.; Elbatal, H.; Wang, P.; Moorefield, C. N.; Newkome, G. R.; Dai, L. Reversible Self-Assembly of Terpyridine-Functionalized Graphene Oxide for Energy Conversion. *Angew. Chem., Int. Ed.* **2014**, *53*, 1415−1419.

(32) Hou, Y.; Huang, T.; Wen, Z.; Mao, S.; Cui, S.; Chen, J. Metal-Organic Framework-Derived Nitrogen-Doped Core-Shell-Structured Porous Fe/Fe$_3$C@C Nanoboxes Supported on Graphene Sheets for Efficient Oxygen Reduction Reactions. *Adv. Energy Mater.* **2014**, *4*, 1220−1225.

(33) Yang, W.; Zhai, Y.; Yue, X.; Wang, Y.; Jia, J. From Filter Paper to Porous Carbon Composite Membrane Oxygen Reduction Catalyst. *Chem. Commun.* **2014**, *50*, 11151−11153.